Bio-Inspired Fiber Attitude Sensor for Direction-Distinguishable Pitching and Rolling Sensing

Jiabin Wang, Xingyu Yang, Anzhi Wang, Hang Jiang, Linbin Bai, Haoran Meng, Song Li, Tao Geng, and Weimin Sun

***Abstract*—Attitude sensors are critical elements in the field of automation control. In this study, we propose and demonstrate a whisker-inspired fiber attitude sensor (WI-FAS) capable of simultaneously measuring pitching and rolling angles. A photopolymerized whisker grows out of the central core of a seven-core fiber (SCF) and holds a solid pendulum. Six parallel Fabry-Perot interferometers formed between the SCF. The pendulum transforms variations in cavity length caused by pitching and rolling into the evolution of the interference signal. A fan-in/fan-out device is used to implement space division multiplexing of the SCF, enabling the proposed sensor to judge direction. We also develop a mathematical expression to explain the association between the pitching and rolling angles and the WI-FAS output signals. Mechanical simulations are carried out to investigate the primary factors that affect the sensitivity. With optimum settings, the proposed WI-FAS achieves continuous and simultaneous monitoring of pitching and rolling with a sensitivity of greater than 0.13 nm/° in the angle range of $-180°$ to $+180°$. The suggested WI-FAS exhibits the advantages of compact size, high sensitivity, and has the ability to monitor pitching and rolling simultaneously. Thus it is a competitive candidate in the field of attitude sensing.**

***Index Terms*—Attitude sensor, bio-inspired, Fabry-Perot interferometers.**

Manuscript received 17 April 2023; revised 28 May 2023; accepted 11 July 2023. Date of publication 13 July 2023; date of current version 2 November 2023. This work was supported in part by the Joint Research Fund in Astronomy under cooperative agreement between the National Natural Science Foundation of China (NSFC) and Chinese Academy of Sciences (CAS) under Grants U2031130 and U2031132, in part by the State Key Laboratory of applied optics under SKLA02022001A02, and in part by the Fundamental Research Funds for the Central Universities to the Harbin Engineering University under Grant 3072022QBZ2501. *(Corresponding author: Tao Geng.)*

This work did not involve human subjects or animals in its research.

Jiabin Wang, Xingyu Yang, Anzhi Wang, Hang Jiang, Song Li, and Weimin Sun are with the Key Laboratory of In-Fiber Integrated Optics of Ministry of Education, Harbin Engineering University, Harbin 150001, China (e-mail: wangjiabin@hrbeu.edu.cn; yangxingyu@hrbeu.edu.cn; wanganzhi@hrbeu.edu.cn; heu_jianghang@126.com; lisong@hrbeu.edu.cn; sunweimin@hrbeu.edu.cn).

Linbin Bai is with the Shanghai Optoweave Technology Co., Ltd., Shanghai 200240, China (e-mail: bai.linbin@optoweave.com).

Haoran Meng is with the Changchun Institute of Optics, Fine Mechanics and Physics, Chinese Academy of Sciences, Changchun 130033, China (e-mail: menghaoran@ciomp.ac.cn).

Tao Geng is with the Key Laboratory of In-Fiber Integrated Optics of Ministry of Education, Harbin Engineering University, Harbin 150001, China, and also with the State Key Laboratory of Applied Optics, Changchun Institute of Optics, Fine Mechanics and Physics, Chinese Academy of Sciences, Changchun 130033, China (e-mail: gengtaohitoe@126.com).

Color versions of one or more figures in this article are available at https://doi.org/10.1109/JLT.2023.3294956.

Digital Object Identifier 10.1109/JLT.2023.3294956

I. Introduction

THE attitude information represents the orientation of an object (such as an airplane) in three-dimensional space, including its pitching, rolling, and yaw angles relative to a specific coordinate system [1]. In the fields of aerospace, intelligent robots, astronomical telescopes, and underwater vehicles, attitude sensors with high sensitivity and direction-distinguishable ability play important roles in estimating the spatial attitude of the carrier [2], [3]. At present, the acquisition of attitude information mainly depends on inertial sensors, magnetometers, machine vision, and the Global Navigation Satellite System (GNSS) [4], [5]. Among these approaches, the inertial sensor which is mounted inside the carrier exhibits attractive advantages of cost efficiency and is unconstrained by the earth's magnetic field and external environment.

In recent years, varieties of inertial attitude sensors including electrical and optical fiber sensors have been designed and verified. The designing framework of these sensors focuses on the construction of pendulum structures. The so-called pendulum can be a solid ball, an air bubble, or a liquid drop. Compared with electrical sensors, fiber attitude sensors have distinct advantages of high sensitivity, immunity to electromagnetic interference, and ease of multiplexing. Fiber Bragg grating (FBG) [6], Mach–Zehnder interferometer (MZI) [7], and Fabry-Perot interferometer (FPI) [8] are the most common frameworks for designing fiber attitude sensors. Micro-pendulums are also integrated with well-designed fiber structures to strengthen the sensing performances of the sensors. In addition, sensors based on polymer fibers also exhibit enhanced performances [9], [10], [11], [12]. However, it is difficult for traditional fiber attitude sensors to meet the requirements of direction identification and simultaneous measurement of pitching angle and rolling angle. Although the FBG array [13] or the FBGs inscribed on multicore fibers [14] can give these sensors the ability to measure both pitching and rolling angles simultaneously, disadvantages of complex structure, large size, and low sensitivity still limit the further development of the attitude sensors with such designing frameworks.

Whiskers are important sensory organs for many animals in nature. The pendulum-shaped whiskers bend or vibrate when external signals such as micro-vibrations or changes in fluid velocity load on them. An abundance of nerve cells in the hair

follicles at the base of the whiskers can sense the change and transmit the signal to the animal's brain. Animals including mice, cats, and harbor seals use whiskers to sense changes in the environment, search for prey, and control body balance. In the field of bionic sensing, whisker-inspired sensors have become a hot research topic. Multifarious whisker-inspired sensors have been designed and applied for underwater acoustic sensing [15], nano newton force measurement [16], and shape recognition [17]. While to the best of our knowledge, there have been few reports on whisker-inspired attitude sensors.

In this article, we propose and demonstrate a compact whisker-inspired fiber attitude sensor (WI-FAS) for direction-distinguishable pitching and rolling sensing. A solid pendulum made up of a short section of single-mode fiber (SMF) is held up by a section of photopolymer whisker which grows from the central core of a seven-core fiber (SCF). Six parallel FPIs formed between the planetary cores of the SCF and the SMF end face play roles of receptors of mammalian follicles systems. Under the action of the SMF pendulum gravity, the whisker bends slightly, resulting in a regular difference in the length of the six air cavities. Therefore, the pitching and rolling angles are able to be calculated by demodulating the output signals of the six bionic receptors. Compared with conventional fiber attitude sensors, the proposed WI-FAS realize the simultaneous measurement of pitching angle and rolling angle with a more compact structure, larger dynamic range, and high sensitivity.

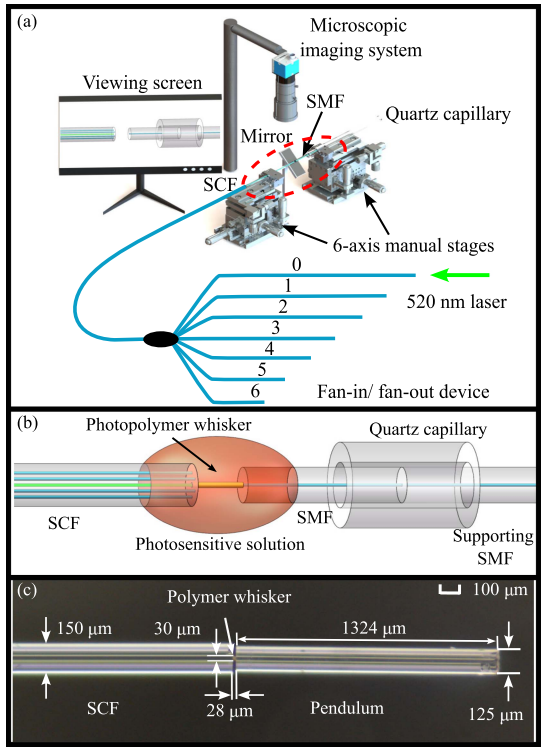

Fig. 1. The schematic diagram of the experimental setup for fabricating the device.

II. Fabrication

The schematic diagram of the experimental setup for fabricating the WI-FAS is shown in Fig. 1(a). Only two steps are required for preparing the WI-FAS.

Firstly, the output SCF of a commercially available fan-in/fan-out device (FIFO) OWMCF-7C542S (Optoweave Co., LTD) is mounted on a 6-axis manual stage (NFP-6561, Zolix Instruments Co., Ltd.) by a fiber clamp. The FIFO has crosstalk between the adjacent core as low as -50 dB which is realized by the channel-assisted low crosstalk fibers. The core diameter and core-to-core distance of the output SCF of the FIFO are 8.2 μm and 42 μm, respectively. The end face of the SCF is well prepared by a fiber cleaver (CT-08, Fujikura Co., Ltd.). A short section of SMF (SMF 28e+, Corning Inc.) with a certain length (L_{SMF}) is obtained with the help of a ruby fiber-cutting pen (FCCP-R, LBTEK Co., Ltd.). It is worth noting that in order to hold the SMF segment stably, we insert it into a quartz capillary with an inner diameter of 200 μm. A supporting SMF is inserted from the other end of the capillary to ensure the stability of the SMF as shown in Fig. 1(b). The quartz capillary holding the SMF is mounted on another 6-axis manual stage through the fiber clamp. The SCF and the SMF are aligned using two-dimensional machine vision. The distance between them which determines the length of the polymer whisker (L_{W}) is accurately controlled by the two 6-axis stages.

Secondly, a photopolymerizable solution is dripped into the space between the SCF and the SMF pendulum. The photopolymerizable solution used here contains a monomer–pentaerythritol triacrylate (PETIA), a sensitizing system – eosin Y, and a methyldiethanolamine [18]. Then a pig-tail-fiber coupled semiconductor laser with a central wavelength of 520 nm is injected into the center core of the SCF through the FIFO. When eosin is irradiated by a 520 nm laser, the triplet state of eosin reacts with the amine to initiate the polymerization of the acrylate monomer [18]. Therefore solid polymer whisker grows from the center core of the SCF and glues to the SMF due to the "self-trapping effect" [19]. The diameter of the polymer whisker (D_{W}) is able to be controlled by adjusting the laser power and exposure time. We note that for a certain length, the diameter of the whisker is mainly determined by the laser power. This is because monomer polymerization occurs only when the laser energy density exceeds the reaction threshold [18]. The output energy field of the optical fiber is the well-known Gaussian-like distribution, and the energy decreases gradually from the center to the edge of the field. Although there are high-order modes in the standard communication SMF, we still obtain an approximate Gaussian-like emission field by means of mechanical scrambling and realize a cylindrical whisker [20]. Higher power increases the diameter of the mode field beyond the threshold of the polymerization reaction, resulting in an increment in the polymer diameter. The exposure time affects the length of the whisker. For longer whiskers, it is necessary to increase the exposure time to allow sufficient polymerization to take place. For practical applications, the diameter and length of the whisker are able to be well designed according to demands.

Finally, the sensor is successfully obtained after washing the unreacted solution off with ethanol. The micrograph of a fabricated WI-FAS is shown in Fig. 1(c). The measured diameter

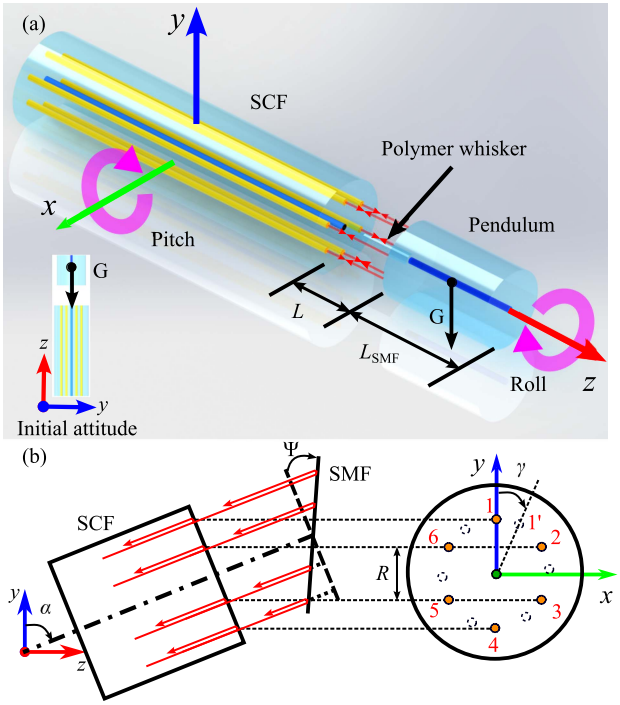

Fig. 2. The schematic diagram of the whisker-inspired fiber attitude sensor. (a) Overall structure diagram; (b) schematic diagram of working principle.

(D_{W}) and length (L_{W}) of the polymer whisker is 30 μm and 28 μm, respectively. The SMF pendulum with a length (L_{SMF}) of 1324 μm is held by the polymer whisker.

III. Sensing Principle and Simulation

The schematic diagram of the WI-FAS is shown in Fig. 2(a). A thin polymer column growing from the central core of the SCF holds up the SMF pendulum. Six parallel FPIs formed between the six planetary cores of the SCF and the end face of the SMF. Such a structure is inspired by the whiskers of mammals. The photopolymer column acts as the animal whisker body. The "sensitive cells" consist of the six parallel FPIs. The signals are finally transmitted to the "brain" through the nerves made up of the SCF and the FIFO.

Referring to Fig. 2(b), the seven cores of the SCF are numbered in the sequence. Among the seven cores, the central core labeled core 0 is used for transmitting the 520 nm laser for inducing the monomer polymerization of acrylate. Broadband light is injected into the six planetary cores labeled core 1 to core 6 respectively through the SMF-input end of the FIFO. Parallel Fabry-Perot interferences occur between the light reflected from the exit end face of each planetary core and the nearby SMF end face. The six FPIs are labeled FPI 1 to FPI 6 in the same order as the core numbers. The interference is able to be approximately regarded as double-beam interference. The output intensity I is mathematically expressed as [21]

$$I = I_1 + I_2 + 2\sqrt{I_1 I_2}\cos(\Delta\phi) \tag{1}$$

where I_1 and I_2 are the intensity of the reflections; $\Delta\phi$ represents the phase difference between the two interferential beams, which is expressed as [21]

$$\Delta\phi = \frac{2\pi}{\lambda} n 2L \tag{2}$$

where L and n refer to the length and refractive index of the cavity, respectively; λ is the central wavelength in vacuum. According to (1) and (2), destructive interference occurs when the phase of the cosine term becomes an odd number of π. Therefore, the central wavelength (λ_m) of the m^{th} order dip of the interference signal is determined by

$$\lambda_m = \frac{4\pi n L}{(2m+1)\pi} \tag{3}$$

Equation (3) indicates that for a certain dip, λ_m is proportional to L. It means that when the cavity is stretched, the target dip shows a redshift.

To describe the working principle of the WI-FAS more clearly, we define the object coordinate system as shown in Fig. 2(a). The pitching angle (α) and rolling angle (γ) represent the rotation of the sensor about the x and z axis of the object coordinate system, respectively. Clockwise rotations are defined as positive angles. In another word, α and γ are in the range of $-180°$ to $+180°$. The initial attitude of the WI-FAS where α and γ are zero is shown in the illustration in Fig. 2(a). In the initial attitude, the sensor is pointing straight up with respect to the inertial coordinate system. And the lines at the center of core 1 and core 4 are parallel to the y-axis of the object coordinate system [seen in Fig. 2(b)].

Under the action of the pendulum gravity, the polymer whisker bends and results in a variation in L of the six FPIs. Such a variation changes with α due to the difference in the angle between the gravity and the support force of the whisker. Meanwhile, the interference signals of the FPIs also evolve with the change of γ for a certain α (except 0° and ±180°). Ignoring the changes in the length of the polymer whisker itself, the cavity length of the n^{th} FPI ($L(n)$) of the WI-FAS when the pitching and rolling angle is α and γ respectively, is able to be expressed as

$$L(n) = L + R\cos[\gamma + (n-1)60°]\tan(\Psi) \tag{4}$$

where n is the core number of the SCF and n = 1, 2, 3, 4, 5, and 6 here; R refers to the adjacent core spacing. It is worth noting that the actual deflection angle of the pendulum SMF [labeled Ψ in Fig. 2(b)] is different from α due to the supporting force of the polymer whisker. Ψ is a function of multiple parameters including the pendulum length (L_{SMF}), the whisker length (L_{W}), and the diameter (D_{W}) and α. Therefore we use Ψ [$\Psi = \Psi(L_{\mathrm{SMF}}, D_{\mathrm{W}}, L_{\mathrm{W}}, \alpha)$] to represent actual deflection angle.

We define the wavelength response function of the n^{th} FPI (F_n) as the wavelength changes of the target dip simultaneously with the pitching and the rolling angle according to (3) and (4). Thus F_n is expressed as

$$F_n = \frac{4}{2m+1}\{L + R\cos[\gamma + (n-1)60°]\tan(\Psi)\} - \lambda_0^n \tag{5}$$

where λ_0^n refers to the target wavelength of the n^{th} FPI when the sensor is in the initial attitude. In the initial attitude, $L = L_{\mathrm{W}}$, and $\lambda_0^n = 4L/(2m+1)$.

TABLE I
THE PARAMETERS USED IN THE SIMULATION

No.	Parameter	Value
1	Fiber density	2700 kg/m^3 [22]
2	Fiber Young's Modulus	72.5 Gpa [22]
3	Fiber Poisson's ratio	0.17 [22]
4	Polymer Young's Modulus	2 Gpa [23]
5	Polymer Poisson's ratio	0.35 [24]
6	Polymer density	1.2 g/cm^3
7	Length of pendulum (L_{SMF})	1300 μm
8	Length of whisker (L_{W})	30 μm
9	Diameter of whisker (D_{W})	30 μm

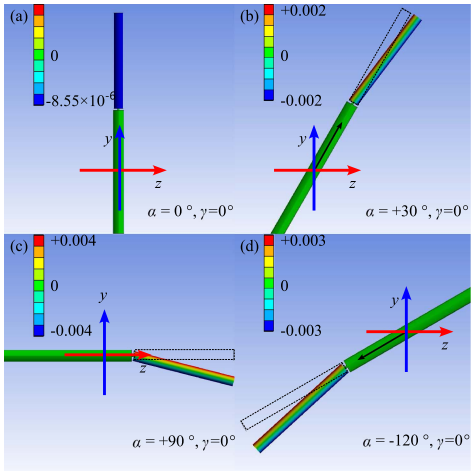

Fig. 3. Deformation of the pendulum along the axial direction of the sensor under different α, (a) $\alpha = 0°$; (b) $\alpha = +30°$; (c) $\alpha = +90°$; (d) $\alpha = -120°$.

In order to characterize the cavity length ($L(n)$) change with α and γ in more detail, simulations based on the finite element method (FEM) are carried out to calculate the deformations of the polymer whisker together with the SMF pendulum under the action of gravity. The parameters used in the simulation are listed in Table I. The initial parameters including L_{SMF}, L_{W}, and D_{W} are set according to the experiences from the exploratory experiment before. These parameters are optimized in the followed simulations.

By changing the gravity direction, we adjust the pitching angle (α) and rolling angle (γ) in the simulation. The simulated deformation of the pendulum along the axial direction of the sensor under different α is shown in Fig. 3. Obviously, the bionic whiskers with high elastic modulus bend under the action of pendulum gravity, resulting in a difference in the cavity length of the six parallel FPIs.

The evolution of $L(n)$ as α changes from $-180°$ to $+180°$ is obtained by tracking the length changes of the six sampling paths (corresponding to the six FPIs) in the model. The result in the case of $\gamma = 0°$ is shown in Fig. 4(a). The change of cavity lengths satisfies a sinusoidal function and varies with the number of the FPI. The maximum change of $L(n)$ is obtained when the α is $\pm 90°$. There exists a neutral plane perpendicular to the direction of gravity and passing through the center of the SCF output end. The cavity length of FPIs far from the neutral

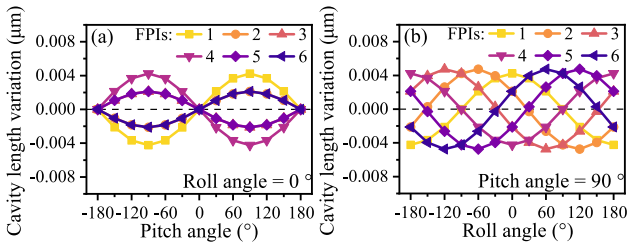

Fig. 4. The cavity length evolution of the six FPIs, (a) α is increased from $-180°$ to $+180°$ while γ is $0°$; (b) γ is increased from $-180°$ to $+180°$ while α is $90°$.

plane changes more than that of FPIs near the neutral plane at any rolling angle. In addition, the cavity-length variation of the FPIs located at the same distance from the neutral plane but on either side of it has the same absolute value but opposite sign.

Similarly, we plot the relationship between the variation of $L(n)$ and the rolling angle γ in Fig. 4(b). The results agree well with (4). For a certain α, the length of all the cavities varies with γ as a sine function. The change of cavity length still depends on its direction of motion relative to the neutral plane (except $\alpha = 0°$ or $90°$).

We use the sinusoidal function to fit the relationship between the cavity length variation of FPI 1 - FPI 6 and α when γ is $0°$. By substituting the six sinusoidal functions into (5), we calculate the theoretical wavelength response (around 1550 nm) to the pitching and rolling angle. The results are shown in the heatmap in Fig. 5.

Obviously, the variation of the target wavelength with both pitching angle α and rolling angle γ satisfies certain sinusoidal functions except for some special cases. For a fixed γ, the six sinusoidal functions have the same initial phase and different amplitudes. When the α is fixed, the amplitudes of the functions are the same but the initial phases differ by $60°$ in turn. This is easy to understand that for the standard weakly-coupled SCF with hexagonal-core distribution, FPI (n) is equivalent to FPI $(n+1)$ or FPI $(n-1)$ for every $60°$ increase or decrease in the rolling angle.

The n^{th} FPI sensitivities of the sensor for pitching and rolling angle measurement are derived according to (5), respectively.

$$\frac{\partial \lambda}{\partial \alpha}(n) = \frac{\lambda_m}{L}\frac{\partial L}{\partial \alpha} = \frac{\lambda_m}{L}\frac{R\cos[\gamma + (n-1)60°]}{\cos^2(\Psi)}\frac{\partial \Psi}{\partial \alpha} \tag{6}$$

$$\frac{\partial \lambda}{\partial \gamma}(n) = \frac{\lambda_m}{L}\frac{\partial L}{\partial \gamma} = -\frac{\lambda_m}{L}R\tan(\Psi)\sin[\gamma + (n-1)60°] \tag{7}$$

Equations (6) and (7) indicate that the pitching and rolling sensitivity is proportional to $\partial L/\partial \alpha$ and $\partial L/\partial \gamma$ respectively for a certain dip of the interference spectrum. Furthermore, the terms R and n are constant. Therefore the term Ψ related to the pendulum length (L_{SMF}), whisker diameter (D_{W}) and length (L_{W}) mainly affects the sensitivity. Here we simulate the pitching and rolling sensitivities through the FEM. In order

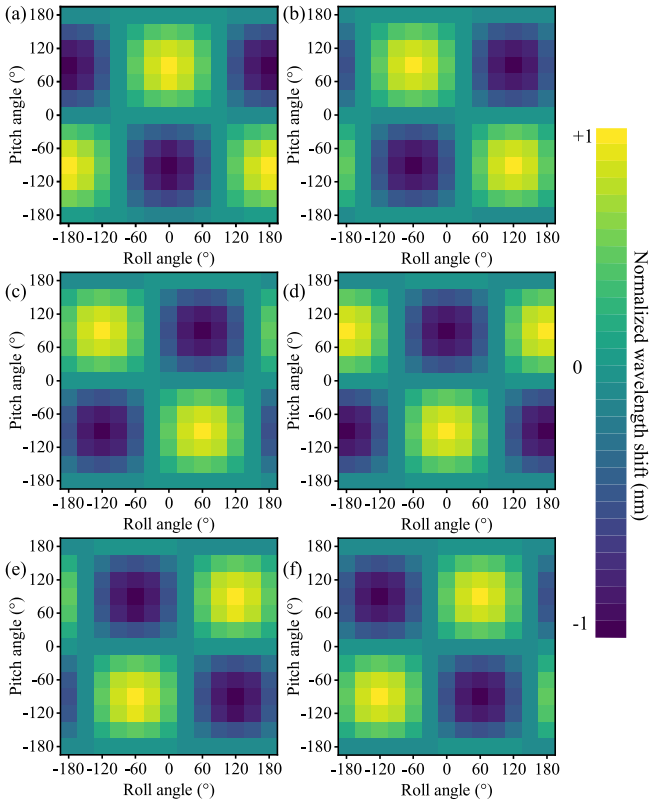

Fig. 5. The simulated wavelength variation of the target dips around communication wavelength with the pitching and rolling angle. (a) FPI 1; (b) FPI 2; (c) FPI 3; (d) FPI 4; (e) FPI 5; (f) FPI 6.

to more clearly show the influence of the three factors on the sensitivity, we calculated the cavity-length variation of FPI 1 (defined in Fig. 2) with the changed factors. We note that the simulation is carried out following the principle of controlling a single variable.

It is seen from Fig. 6 that the WI-FAS with a longer pendulum, and longer and thinner whisker exhibit higher pitching and rolling sensitivities. Among the three factors, the diameter of the polymer whisker (D_{W}) has the greatest influence on sensitivity, followed by whisker length (L_{W}) and pendulum length (L_{SMF}). However, an overhigh sensitivity also means that the stability and repeatability of the device are weak. Besides, L_{SMF} is hard to control precisely by manually cutting. Thus the sensitivity of the suggested WI-FAS mainly depends on the geometric parameters of the whisker.

According to the simulation results, the theoretical optimization parameters are $L_{\mathrm{SMF}} = 1300\ \mu$m, $L_{\mathrm{W}} = 30\ \mu$m, and $D_{\mathrm{W}} = 30\ \mu$m by taking into account the structural stability of the device.

IV. Experimental Results and Discussions

According to the detailed theoretical analysis and simulation results in Section III, a sample with L_{SMF} of 1324 μm, L_{W} of 28 μm, and D_{W} of 30 μm is fabricated. The sensor is mounted on a testing setup and adjusted to be in the initial state ($\alpha = 0°, \gamma = 0°$) defined in Fig. 2. The schematic diagram of the testing setup is shown in Fig. 7. A fiber rotator (HFR-007, Thorlabs Inc.)

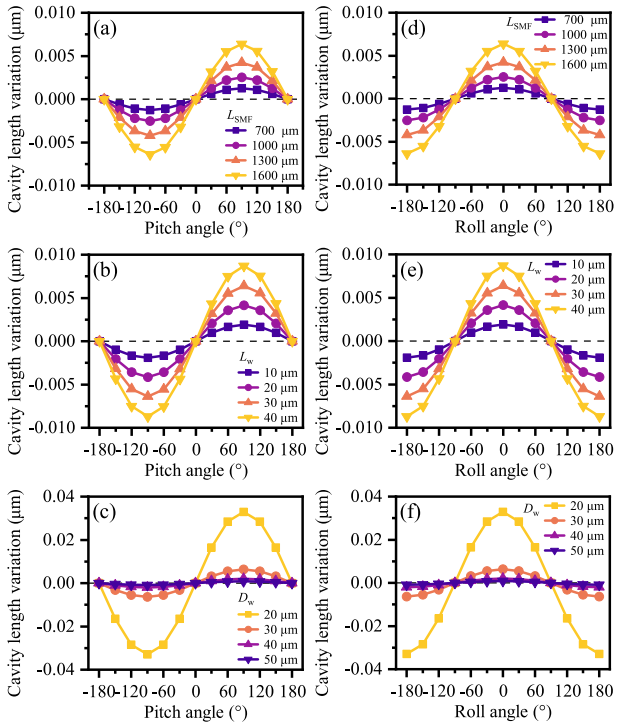

Fig. 6. (a), (b), and (c) The influences of L_{SMF}, L_{W}, and D_{W} on pitching angle sensitivity; (d), (e), and (f) The influences of L_{SMF}, L_{W}, and D_{W} on rolling angle sensitivity.

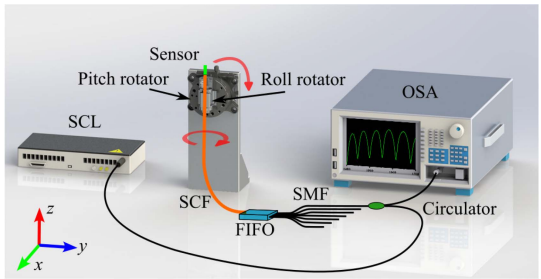

Fig. 7. Experimental setup for measuring the pitching and rolling.

mounted on a rotation stage (RP-1A-KIT, LBTEK Co., Ltd.) holds the WI-FAS and controls the rolling angle γ. The manual rotation stage fixed in the vertical plane determines the pitching angle α of the sensor. A supercontinuum laser source (SCL) SC-5 (YSL Photonics Co., Ltd) feeds the sensor with broadband light ranged 1400 nm- 1700 nm through a fiber circulator and the FIFO. The interference signals of the six parallel FPIs return to the circulator along the corresponding core of the SCF and are recorded by an optic spectral analyzer (OSA) AQ6370D (YOKOGAWA Co., Ltd) with a resolution of 0.2 nm.

The initial spectra of the six parallel FPIs are collected and shown in Fig. 8(a). We use color mapping to represent the transmission. It is seen from Fig. 8(a) that the spectra of the six FPIs show a satisfactory consistency in the waveform. We have to point out that the extinction ratio (ER) of the dips obtained from different FPIs is slightly different. The ER is determined by

$$K = 2\sqrt{I_1 I_2}/(I_1 + I_2) \tag{8}$$

TABLE II
THE SINUSOIDAL FITTING RESULTS OF THE RELATIONSHIP BETWEEN THE WAVELENGTH VARIATION AND THE PITCH AND ROLL ANGLES

Number	Pitching angle responses (γ=0°)	R^2	Rolling angle responses (α=90°)	R^2
FPI 1	$P_1 = 0.02 + 7.88\sin((\alpha + 2.26)\pi/182.98)$	0.99	$R_1 = -0.06 + 6.83\sin((\gamma + 88.93)\pi/178.83)$	0.99
FPI 2	$P_2 = -0.24 + 3.67\sin((\alpha + 5.66)\pi/179.20)$	0.98	$R_2 = 2.26 + 7.93\sin((\gamma - 203.61)\pi/179.39)$	0.99
FPI 3	$P_3 = -0.42 + 4.70\sin((\alpha - 240.00)\pi/201.45)$	0.99	$R_3 = -1.30 + 7.97\sin((\gamma - 141.48)\pi/178.95)$	0.99
FPI 4	$P_4 = -0.55 + 8.24\sin((\alpha - 195.25)\pi/194.29)$	0.99	$R_4 = 0.01 + 7.37\sin((\gamma - 81.21)\pi/179.49)$	0.99
FPI 5	$P_5 = -0.25 + 3.47\sin((\alpha - 200.75)\pi/201.28)$	0.99	$R_5 = -2.38 + 7.40\sin((\gamma - 21.78)\pi/180.05)$	0.99
FPI 6	$P_6 = -0.04 + 4.39\sin((\alpha + 1.45)\pi/178.27)$	0.98	$R_6 = 0.99 + 6.98\sin((\gamma + 40.58)\pi/180.52)$	0.99

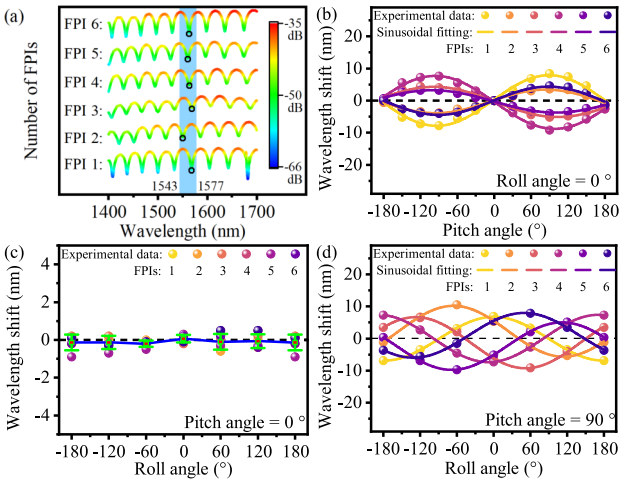

Fig. 8. (a) The interference spectra of the six FPIs of the WI-FAS; the target wavelength evolution with the (b) pitching angle ($\gamma = 0°$); (c) rolling angle ($\alpha = 0°$); (d) rolling angle ($\alpha = 90°$).

Equation (8) indicates that ER is influenced by the intensity of the two beams involved in the interference. For the WI-FAS, I_1 and I_2 are mainly affected by the reflectivity of the fiber end face. Therefore we can say the ER difference of the six interference signals is caused by the difference in surface flatness caused by manual cutting. The average ER of the six spectra is 13.61 dB. The difference in the wavelength of the dips between the FPIs is caused by the different initial phases. Such an initial phase difference is an inherent property of the SCF, which is caused by the tiny refractive index difference between the cores formed during the fabrication. Considering the compatibility with commercial instruments and ease of demodulation, we focus on the dips located around 1550 nm as marked by circles in Fig. 8(a).

Then we characterize the pitching and rolling responses of each FPI of the WI-FAS, respectively. The angles are changed from 0° to +180° and −180° with a step of 30° by rotating the pitching or rolling rotator. The pitching angle responses are tested under a fixed γ of 0° (seen in Fig. 8(b)). The rolling angle responses under the α of 0° (seen in Fig. 8(c)) and 90° (seen in Fig. 8(d)) are also tested. The wavelength evolution of the target dips with α and γ is obtained by tracing the interference signals. According to the theoretical analysis in Section III, sinusoidal functions are applied to fit the relationship between the wavelength evolution and the angles. The fitted sinusoidal functions and the corresponding goodness of fitting (R^2) are listed in Table II. We note that when $\alpha = 0°$, the target wavelengths are almost unchanged with γ. Therefore the results are only shown by a dot plot with error bars without fitting.

TABLE III
THE RESPONSE FUNCTIONS OF THE SIX FPIS OF THE SENSOR TO PITCHING ANGLE AND ROLLING ANGLE SIMULTANEOUSLY

Number	Response functions
FPI 1	$F_1 = \cos(0.0175\gamma)\,[7.88\sin(0.0172\alpha + 0.0387) + 0.0243]$
FPI 2	$F_2 = 2\cos(0.0175\gamma + 1.05)\,[3.67\sin(0.0175\alpha + 0.0992) - 0.241]$
FPI 3	$F_3 = -2\cos(0.0175\gamma + 2.09)\,[4.70\sin(0.0560\alpha - 3.74) - 0.419]$
FPI 4	$F_4 = -\cos(0.0175\gamma + 3.14)\,[8.24\sin(0.0162\alpha - 3.16) - 0.550]$
FPI 5	$F_5 = -2\cos(0.0175\gamma + 4.19)\,[3.47\sin(0.0156\alpha - 3.13) - 0.254]$
FPI 6	$F_6 = 2\cos(0.0175\gamma + 5.24)\,[4.39\sin(0.0176\alpha + 0.0256) - 0.0420]$

The experimental results agree well with the simulation. When the rolling angle γ is 0°, FPI 1 and FPI 4 exhibit the highest sensitivity. The amplitude of their fitting functions is almost the same. The slight difference between the functions of FPI 2 and FPI 6 as well as FPI 3 and FPI 5 is caused by the imperceptible airflow in the laboratory or the unstable mechanical positioning.

We substitute the fitting functions of pitching angle responses shown in Table II into (5) to obtain the response functions of the six FPIs of the WI-FAS to pitching angle and rolling angle simultaneously. The term γ in (5) is 0. The results are shown in Table III.

We use a heat map to plot the response function listed in Table III when the α and γ range from −180° to +180° [seen in Fig. 9]. Regarding Figs. 5 and 9, the responses of the six parallel FPI to simultaneous variation of pitching and rolling angles obtained by experiment are in good agreement with theoretical analysis and simulation. When α is 0°, the target wavelength hardly shift with γ according to Fig. 9. This is consistent with the experimental results shown in Fig. 8(c). And when α is 90°, the central wavelengths of the six target dips all conform to sine functions. But the initial phases of the six functions differ by 60° in turn. The results derived from the experimentally obtained response functions are proofed by the independent experimental results shown in Fig. 8(d).

To estimate the pitching and rolling angle sensing sensitivity, we take the partial derivatives of the response functions listed in Table III with respect to α and γ respectively. Here we only give the results of FPI 1 to represent the sensing performance of the WI-FAS. The pitching and rolling angle sensitivities are expressed as

$$S_1|_\alpha = |0.135\cos(0.0172\alpha + 0.0387)\cos(0.0175\gamma)| \quad (9)$$

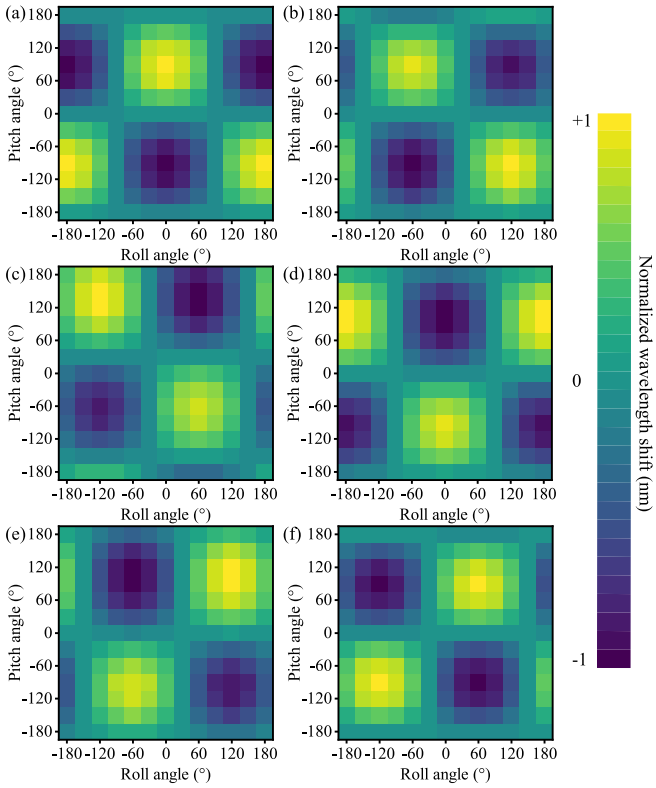

Fig. 9. The experimental wavelength variation of the target dips with pitching and rolling angles obtained by plotting response functions listed in Table III in the α and γ range of $-180°$–$+180°$.(a) FPI 1; (b) FPI 2; (c) FPI 3; (d) FPI 4; (e) FPI 5; (f) FPI 6.

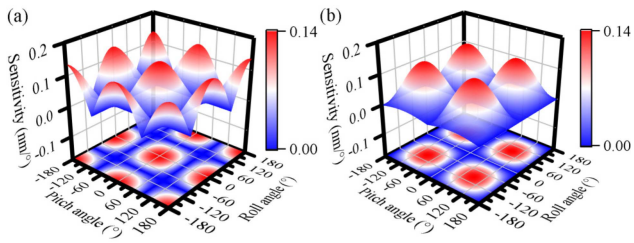

Fig. 10. (a) Pitching angle sensitivities vary with α and γ; (b) rolling angle sensitivities vary with α and γ.

$$S_1|_\gamma = |0.137[\sin(0.0172\alpha+0.0387)+0.0031]\sin(0.0175\gamma)| \tag{10}$$

where $S_1|_\alpha$ and $S_1|_\gamma$ represent the pitching angle sensitivity and rolling angle sensitivity, respectively. In the angles range of $[-180°, +180°]$, the pitching and rolling angle sensitivities varies with α and γ. The results are shown in Fig. 10.

The WI-FAS exhibits the highest pitching angle sensitivity of 0.135 nm/° when α and γ is around $0°, \pm 180°$. The maximum rolling angle sensitivity of 0.137 nm/° appears when α and γ are around $\pm 90°$. However, according to the theoretical analysis shown in Fig. 4, the highest pitching and rolling sensitivity are the same. Here the experimental result shows that there is a sensitivity difference lower than 0.002 nm/°. This can be attributed to the poor positioning accuracy of the test system or the impact of small vibrations of the environment on the WI-FAS. Nevertheless, we can still conclude that the attitude angle sensitivity of the proposed WI-FAS is better than 0.13 nm/°.

TABLE IV
THE SENSING PERFORMANCES COMPARISON BETWEEN THE WI-FAS AND OTHER ATTITUDE SENSORS

Reference	Simultaneous measurement of pitching and rolling angle	Sensitivity (nm/°)	Measurement range (°)	Sensor size (mm)
[6]	No	0.01	0–+90	12×12×78
[7]	No	0.01& 0.005	−90–+90	382×3×650
[8]	No	0.0927	−90–+90	6×0.06×0.06
[25]	No	0.074	0–+20	50×50×280
[26]	No	0.192	−15–+15	160×180×180
[1]	Yes	Not mentioned	0–+50&0–360	40×40×45
Present work	**Yes**	**≥ 0.13**	**−180–+180**	**1.6×0.15×0.15**

The sensing performances of the proposed WI-PAS are compared with that of other fiber optic attitude sensors reported recently, as shown in Table IV. The proposed WI-FAS shows competitive advantages in terms of sensing performances and device size. Compared with the attitude sensors based on the fiber grating and mode interferometer frameworks in [6], [7], [8], [25], WI-FAS not only has a much more compact size but also exhibits excellent sensing performances in terms of much higher sensitivity and wider dynamic range. Although the reported angular sensitivity in [26] is higher than the WI-FAS, the narrow dynamic range is still the bottleneck of such a designing framework which using the gravity of a solid pendulum to stretch FBG array. In addition, benefiting from the space division multiplexing capability of the SCF, the WI-FAS is able to realize continuous monitoring of the pitching angle and rolling angle simultaneously, which makes WI-FAS stand out from these competitors.

V. CONCLUSION

In summary, we propose a whisker-inspired fiber attitude sensor (WI-FAS) based on parallel FPIs for direction-distinguishable pitching and rolling angle sensing. Inspired by the whiskers of mammals, we use a photopolymerisable solution to grow a size-controllable artificial whisker on the end face of the central core of an SCF. A short section of SMF is held by the photopolymer column and acts as a solid pendulum. Six parallel FPIs formed due to the existence of the air cavity between the SCF and the SMF and play roles of "sensitive cells" in the whisker follicles. Static structural mechanics analysis based on FEM indicates that among the three parameters including the whisker diameter (D_{W}) and length (L_{W}) and SMF pendulum length (L_{SMF}), the whisker diameter has the largest nonlinear effect on the device sensitivity, followed by the whisker diameter and pendulum length. Based on the simulation results, WI-FAS with a set of optimized parameters is fabricated and characterized. The experimental results agree well with the theoretical analysis and simulations. In the angle range of $-180°$ to $+180°$, we successfully demonstrated the ability of WI-FAS

to continuously and simultaneously monitor changes in pitching and rolling angles by tracing the interference signals. The angle sensing sensitivity is better than 0.13 nm/°. In addition, a theoretical model for calculating the spectral evolution with pitching and rolling angles is developed and confirmed by experiment. Owing to the advantages of compact size, direction-distinguished ability, high sensitivity, and simultaneous measurement of pitching and rolling angle, the novel WI-FAS is promising in the fields requiring real-time attitude monitoring.

REFERENCES

[1] Y. Liu, S. Chen, Z. Liu, J. Guang, and W. Peng, "Fiber-optic evanescent-field sensor for attitude measurement," *Smart Mater. Struct.*, vol. 26, no. 11, 2017, Art. no. 115018.

[2] J. C. Fang, S. Q. Zheng, and B. C. Han, "Attitude sensing and dynamic decoupling based on active magnetic bearing of MSDGCMG," *IEEE Trans. Instrum. Meas.*, vol. 61, no. 2, pp. 338–348, Feb. 2012.

[3] C. Marques, A. Leal-Junior, and S. Kumar, "Multifunctional integration of optical fibers and nanomaterials for aircraft systems," *Mater.*, vol. 16, no. 4, 2023, Art. no. 1433. [Online]. Available: https://www.ncbi.nlm.nih.gov/pubmed/36837063

[4] C. M. Yu et al., "Angular rate measurement method of magnetically suspended control and sensing gyroscope using component-level rotation modulation," *IEEE Sensors J.*, vol. 22, no. 22, pp. 21575–21584, Nov. 2022.

[5] M. K. Wu, Y. He, S. Luo, and W. K. Liu, "Particle filter-based real-time phase line bias estimation for GNSS-based attitude determination with common-clock receivers," *Adv. Space Res.*, vol. 71, no. 3, pp. 1682–1699, 2023.

[6] N. N. Ismail et al., "Novel 3D-printed biaxial tilt sensor based on fiber Bragg grating sensing approach," *Sensors Actuators A- Phys.*, vol. 330, 2021, Art. no. 112864.

[7] A. S. Sharbirin et al., "3D-printed tilt sensor based on an embedded two-mode fiber interferometer," *IEEE Sensors J.*, vol. 21, no. 6, pp. 7565–7571, Mar. 2021.

[8] C. Lang, J. Zhu, Y. Liu, Y. Li, and S. Qu, "Ultra-compact full-angle-range direction-distinguishable tilt sensor based on fiber in-line polymer microcavity," *J. Lightw. Technol.*, vol. 40, no. 9, pp. 3084–3089, May 2022.

[9] R. Min, B. Ortega, and C. Marques, "Fabrication of tunable chirped MPOF Bragg gratings using a uniform phase mask," *Opt. Exp.*, vol. 26, no. 4, pp. 4411–4420, 2018.

[10] A. Leal-Junior, J. Casas, C. Marques, M. J. Pontes, and A. Frizera, "Application of additive layer manufacturing technique on the development of high sensitive fiber Bragg grating temperature sensors," *Sensors*, vol. 18, no. 12, 2018, Art. no. 4120.

[11] C. Broadway, R. Min, A. G. Leal-Junior, C. Marques, and C. Caucheteur, "Toward commercial polymer fiber Bragg grating sensors: Review and applications," *J. Lightw. Technol.*, vol. 37, no. 11, pp. 2605–2615, Jun. 2019.

[12] A. G. Leal-Junior et al., "Polymer optical fiber for angle and torque measurements of a series elastic actuator's spring," *J. Lightw. Technol.*, vol. 36, no. 9, pp. 1698–1705, May 2018.

[13] K. Ni, X. Y. Dong, Y. X. Jin, and H. S. Xu, "Temperature-independent fiber Bragg grating tilt sensor," *Microw. Opt. Technol. Lett.*, vol. 52, no. 10, pp. 2250–2252, 2010.

[14] W. N. MacPherson et al., "Pitch and roll sensing using fibre Bragg gratings in multicore fibre," *Meas. Sci. Technol.*, vol. 15, no. 8, pp. 1642–1646, 2004.

[15] S. Y. Wang et al., "Underwater bionic whisker sensor based on triboelectric nanogenerator for passive vortex perception," *Nano Energy*, vol. 97, 2022, Art. no. 107210.

[16] M. Q. Zou et al., "Fiber-tip polymer clamped-beam probe for high-sensitivity nanoforce measurements," *Light- Sci. Appl.*, vol. 10, no. 1, 2021, Art. no. 171.

[17] Q. Jiang, G. Z. Wei, and C. L. Zhao, "Fiber Bragg grating-based biomimetic whisker for shape and texture recognition," *J. Instrum.*, vol. 13, 2018, Art. no. P11013.

[18] A. Espanet, C. Ecoffet, and D. J. Lougnot, "PEW: Photopolymerization by evanescent waves. II. Revealing dramatic inhibiting effects of oxygen at submicrometer scale," *J. Polym. Sci. Part A: Polym. Chem.*, vol. 37, no. 13, pp. 2075–2085, 1999.

[19] P. Gustafik, O. Sugihara, and N. Okamoto, "Optical properties of acrylate-based negative-typephotoresist and its application to optical waveguide fabrication," *Japanese J. Appl. Phys.*, vol. 43, no. 4S, 2004, Art. no. 2011.

[20] L. M. Xiao, W. Jin, and M. S. Demokan, "Photopolymer microtips for efficient light coupling between single-mode fibers and small-core photonic crystal fibers," *Proc. SPIE*, vol. 6379, pp. 10–19, 2006.

[21] S. Liu et al., "High-sensitivity strain sensor based on in-fiber improved fabry-perot interferometer," *Opt. Lett.*, vol. 39, no. 7, pp. 2121–2124, 2014.

[22] C. P. Lu et al., "High torsion sensitivity sensor based on LPFG with unique geometric structure," *IEEE Sensors J.*, vol. 21, no. 5, pp. 6217–6223, Mar. 2021.

[23] M. Belqat et al., "Tuning nanomechanical properties of microstructures made by 3 D direct laser writing," *Additive Manuf.*, vol. 47, 2021, Art. no. 102232.

[24] H. Gojzewski, M. Sadej, E. Andrzejewska, and M. Kokowska, "Dataset for acrylate/silica nanoparticles formulations and photocured composites: Viscosity, filler dispersion and bulk poisson's ratio," *Data Brief*, vol. 12, pp. 528–534, 2017. [Online]. Available: https://www.ncbi.nlm.nih.gov/pubmed/28516149

[25] R. G. Yang, H. L. Bao, S. Q. Zhang, K. Ni, Y. Z. Zheng, and X. Y. Dong, "Simultaneous measurement of tilt angle and temperature with pendulum-based fiber Bragg grating sensor," *IEEE Sensors J.*, vol. 15, no. 11, pp. 6381–6384, Nov. 2015.

[26] S. L. He, X. Y. Dong, K. Ni, Y. X. Jin, C. C. Chan, and P. Shum, "Temperature-insensitive 2 D tilt sensor with three fiber Bragg gratings," *Meas. Sci. Technol.*, vol. 21, no. 2, 2010, Art. no. 025203.